The Journal of Chemical Physics

High resolution two-dimensional infrared (HR-2DIR) spectroscopy of gas phase molecules

Cite as: J. Chem. Phys. **157**, 184201 (2022); https://doi.org/10.1063/5.0109084
Submitted: 11 July 2022 • Accepted: 10 October 2022 • Accepted Manuscript Online: 12 October 2022 • Published Online: 14 November 2022

DeAunna A. Daniels, Thresa A. Wells and Peter C. Chen

AIP Publishing

The Journal of Chemical Physics ARTICLE scitation.org/journal/jcp

High resolution two-dimensional infrared (HR-2DIR) spectroscopy of gas phase molecules

Cite as: J. Chem. Phys. 157, 184201 (2022); doi: 10.1063/5.0109084
Submitted: 11 July 2022 • Accepted: 10 October 2022 •
Published Online: 14 November 2022

DeAunna A. Daniels, Thresa A. Wells, and Peter C. Chen[a)]

AFFILIATIONS

Department of Chemistry and Biochemistry, Spelman College, 350 Spelman Lane SW, Atlanta, Georgia 30314, USA

Note: This paper is part of the JCP Special Topic on Celebrating 25 Years of Two-Dimensional Infrared (2D IR) Spectroscopy.
[a)]**Author to whom correspondence should be addressed:** pchen@spelman.edu

ABSTRACT

Two-dimensional infrared (2DIR) spectroscopy has become an established method for generating vibrational spectra in condensed phase samples composed of mixtures that yield heavily congested infrared and Raman spectra. These condensed phase 2DIR spectrometers can provide very high temporal resolution (<1 ps), but the spectral resolution is generally insufficient for resolving rotational peaks in gas phase spectra. Conventional (1D) rovibrational spectra of gas phase molecules are often plagued by severe spectral congestion, even when the sample is not a mixture. Spectral congestion can obscure the patterns in rovibrational spectra that are needed to assign peaks in the spectra. A method for generating high resolution 2DIR spectra of gas phase molecules has now been developed and tested using methane as the sample. The 2D rovibrational patterns that are recorded resemble an asterisk with a center position that provides the frequencies of both of the two coupled vibrational levels. The ability to generate easily recognizable 2D rovibrational patterns, regardless of temperature, should make the technique useful for a wide range of applications that are otherwise difficult or impossible when using conventional 1D rovibrational spectroscopy.

INTRODUCTION

Infrared spectroscopy has long been one of the most widely used techniques for determining the identity and structure of a molecule. As a conventional 1D spectroscopic technique, however, its capabilities become severely degraded if the sample consists of a mixture. Two dimensional infrared spectroscopy (2DIR) has become a well-established technique for its ability to use the coupling between vibrational peaks in order to overcome the limitations of conventional 1D IR spectroscopy. Recent bioanalytical applications include studying the structure of proteins[1] and unfolded peptides,[2] rapid screening of DNA-ligand complexes,[3] and detection of drug-binding to target proteins.[4] 2DIR has recently been used for studies involving molecular structures and dynamics on surfaces,[5–7] total internal reflection,[8] microscopy,[9] polaritons,[10–12] ionic liquids,[13] crystallography,[14] and photocatalyzed reaction dynamics.[15] The technique has also been expanded to permit three dimensional vibrational spectroscopy.[16–18]

Despite its success in the condensed phase, the use of 2DIR spectroscopy to study freely rotating gas phase molecules has remained largely unexplored. High resolution coherent 2D spectroscopy (HRC2DS) for probing electronic resonances in gas phase molecules with rotational resolution[19] has been developed and produces peaks that assemble into easily recognizable 2D patterns such as an X-shape[20] or a double parabola.[21–23] Pure rotational 2D spectroscopy of gas phase molecules has been described theoretically by Suzuki and Tanimura[24] and demonstrated experimentally by Nelson and co-workers.[25,26] The theory and potential use of frequency combs for 2DIR spectroscopy of gas phase molecules have very recently been described by Kowzan and Allison.[27,28] 2DIR spectra have been recorded in supercritical fluids[29] that show the same overall X-shape[19] previously observed in the gas phase.[22] However, the individual rovibrational peaks in the supercritical fluid 2DIR spectra were not resolved. One issue is that the types of lasers used for many 2DIR experiments employ femtosecond pulse lengths that provide excellent temporal resolution, but their linewidths are too broad to spectrally resolve the rovibrational structure in gas phase samples. By contrast, nanosecond pulsed lasers provide narrower bandwidths that are better suited for gas phase work. Many 2DIR experiments employ time-domain 2D Fourier transform spectroscopy methods

where the spectral resolution is controlled not by the bandwidth of the laser pulses but instead by the varied time delay between pulses. These time domain systems were designed for condensed phase applications, where high temporal resolution may be more important than high spectral resolution. However, the optical delays required to achieve the high spectral resolution needed for gas phase samples would need to be much longer relative to those currently used in condensed phase samples. Furthermore, femtosecond pulses are orders of magnitude shorter than gas phase dephasing times and provide very little time for the coherent signal to build, resulting in signals that could be weak.[30]

In this paper, we demonstrate how to generate rotationally resolved 2DIR spectra of gas phase molecules using a combination of narrowband and broadband nanosecond laser pulses in the infrared region to generate purely coherent four wave mixing (FWM) signals. The spectra are inherently off-diagonal because the narrowband and broadband pulses cover different regions of the infrared spectrum, and the output beam is easily detected because it is in the visible region. This method allows one to scan over regions of the infrared that contain large numbers of peaks while recording a 2D spectrum that contains a smaller subset of coupled peaks in a few tens of minutes. Like previously recorded high resolution coherent multidimensional spectroscopies (HRCMDS) based upon electronic resonances, these observed rovibrational peaks are assembled into easily recognizable patterns that automatically sort peaks by their quantum numbers. The patterns also make it possible to determine molecular constants (vibrational and rotational) and the identity of the FWM process responsible for generating the peaks. This approach could, therefore, be useful for assigning rotational and vibrational quantum numbers in molecular systems that are otherwise difficult or impossible to assign.

BACKGROUND

Compared to condensed phase IR spectroscopy, gas phase IR spectra contain peaks that are many orders of magnitude narrower in linewidth and many orders of magnitude greater in number and density. For example, consider methane, the simplest hydrocarbon with only five atoms and $3N - 6 = 9$ vibrational degrees of freedom. Methane's tetrahedral geometry makes it relatively simple to model compared to other hydrocarbons because spherical rigid rotors are described by just one rotational quantum number and one rotational constant. Furthermore, methane only has four fundamental vibrational frequencies: six modes are triply degenerate [ν_3 (F2) = 3013 cm^{-1} and ν_4 (F2) = 1311 cm^{-1}], two are doubly degenerate [ν_2 (E) = 1533 cm^{-1}], and one is nondegenerate [ν_1 (A1) = 2920 cm^{-1}]. However, the HITRAN database includes more than 90 000 rovibrational peaks for methane between 1100 and 3200 cm^{-1}. For methane, the rovibrational spectrum is complicated due to a high degree of vibrational degeneracy and the similarity in frequencies among ν_1, ν_3, $2\nu_2$, and $2\nu_4$, which lead to a polyad structure extending throughout the near infrared region of the spectrum. Additional factors such as anharmonicity and Coriolis effects further complicate the ability to locate patterns needed to assign methane's rovibrational peaks. This problem is even worse in the near infrared regions, where the large number of poorly characterized interactions affect peak intensities. Such effects on intensity are especially problematic for 1D spectroscopies, where intensities and peak positions are key for pattern identification and peak assignment.

The challenges involved in interpreting the rovibrational spectrum of methane are not unique; severe congestion and complexity are commonly encountered when recording conventional (1D) rovibrational spectra of most gas phase molecules at room temperature. One widely used approach has been to use cryogenic cooling (i.e., molecular jet) to drastically remove most of the rotational peaks. However, such techniques do not work for practical applications where the sample needs to be at higher temperatures. These applications include probing chemical reactions and the analysis of spectra from planetary atmospheres. Alternative approaches to overcoming severe congestion and finding patterns include double resonance spectroscopy and the use of Loomis-Wood plots for trial-and-error post-processing of data.

During the past two decades, HRC2DS techniques have been developed that make use of multiple resonances and multidimensional plots where peaks are automatically sorted into easily recognizable patterns. These techniques have been highly effective for gas phase molecules and mixtures that otherwise yield patternless spectra due to severe spectral congestion. HRC2DS was originally developed for and applied to the rotationally-resolved electronic spectroscopy of diatomic molecules.[21,24] 3D techniques were later added in order to deal with the higher levels of congestion and complexity expected with polyatomic molecules.[31–33] The capabilities of these techniques include the following. First, the expansion to higher dimensions (1D → 2D and 2D → 3D) helps in increasing the spacing between peaks and reducing the peak overlap. Peaks that appear overlapped in one dimension may be clearly resolved in an orthogonal dimension and will, therefore, appear to be clearly resolved in a 2D or higher dimensional plot. Furthermore, peaks produced by similar species, quantum numbers, and selection rules are automatically grouped into easily recognizable 2D patterns (parabolas, X's, squares, triangles, etc.), depending upon the selection rules and technique. The center x,y position of these patterns in 2D spectra yields two separate resonance frequencies on orthogonal axes from two coupled levels and can be used to help distinguish peaks associated with different species[25] or vibrational/vibronic levels. In addition, the spacing between peaks within each 2D pattern helps in providing rotational constants and facilitating the ability to distinguish between patterns from different molecules, which can be useful if the sample is a mixture. Expansion into the third dimension provides additional capabilities, such as selectivity where the observed peaks come from a single selected species in a mixture[34] and more advanced 3D pattern recognition and pattern-generating techniques.[35]

Extending these capabilities to 2DIR could give insight into the detailed structure and behavior of gas phase molecules, facilitate the assignment of rovibrational peaks that have resisted analysis, and provide the ability to analyze gaseous mixtures *in situ*. The infrared region is attractive because of the relationship between vibrational frequencies and functional groups, which is why it is so commonly used for studying organic molecules. Several different methods for generating 2DIR spectra have been developed, including fully coherent frequency domain methods such as Doubly Vibrationally Enhanced (DOVE) spectroscopy[36,37] and time-domain 2DIR pump-probe methods.[38] One reason the DOVE method is especially attractive for high resolution gas phase spectroscopy is that it generates an output signal in the visible region where CCD array detectors can be used to record spectra with high sensitivity. When coupled

with monochromators, commercial systems can resolve visible wavelengths that differ by less than a picometer. DOVE spectra may also be simpler to interpret because they would contain rovibrational peaks from purely coherent processes rather than from a mixture of both population and coherent processes.

Prior work on DOVE by Zhao and Wright has shown that peaks are produced by two different four wave mixing (FWM) processes: a parametric process called DOVE-Raman and a nonparametric process called DOVE-IR.[39] The FWM diagrams for these processes are shown in Fig. 1. In both diagrams, levels b and c can be rovibrational levels of fundamental vibrations, combination bands, or overtones. The intensities of the generated output beam are proportional to the product of the input laser frequencies times the squared modulus of the third order nonlinear susceptibilities, which are described in the following equation for the DOVE-Raman process:

$$\chi^{(3)} = \frac{\mu_{ac}\mu_{cb}\mu_{bd}\mu_{da}}{\Delta_{ca}\Delta_{ba}\Delta_{da}} \tag{1}$$

and in the following equation for the DOVE-IR process:[35]

$$\chi^{(3)} = \frac{-\mu_{ab}\mu_{ac}\mu_{cd}\mu_{db}}{\Delta^{*}_{ba}\Delta_{ca}}\left[\frac{1}{\Delta_{da}} + \frac{i\Gamma^{a}_{cb}}{\Delta_{cb}\Delta_{db}} - \frac{i\Gamma^{a}_{db}}{\Delta_{da}\Delta_{db}}\right], \tag{2}$$

where for the ji transition, μ_{ji} is the transition dipole moment, Δ_{ji} is the resonance denominator ($\Delta_{ji} = \omega_{ji} - \omega_{lasers} - i\Gamma_{ji}$), and ω_{ji} is the difference in frequency between levels j and i in units of cm^{-1}. ω_{lasers} is the combination of laser frequencies required for achieving resonance, Δ^{*}_{ji} is the complex conjugate of Δ_{ji}, and Γ_{ji} is the linewidth in units of cm^{-1}. This linewidth depends upon both the population relaxation rate and pure dephasing,

$$\Gamma_{ji} = \frac{\Gamma_{jj} + \Gamma_{ii}}{2} + \Gamma^{*}_{ji}. \tag{3}$$

In the absence of pure dephasing, $\Gamma^{a}_{ji} = \Gamma^{*}_{ji} - \Gamma^{*}_{ja} - \Gamma^{*}_{ia} - \Gamma_{aa}$ approaches Γ_{aa}, which is typically zero, and the last two bracketed terms in Eq. (2) can be neglected.

For the DOVE-IR process, if level b is an IR-active fundamental vibration, the intensity of the FWM process will increase as the frequency of ω_2 approaches ω_{ba}, the difference in frequency between levels a and b. In a 1,2 plot where the intensity of the FWM signal is plotted as a function of ω_1 along the x-axis and ω_2 along the y-axis, Δ^{*}_{ba} in Eq. (2) predicts a ridge of maximum intensity running horizontally along the 2D plot (see the top left quadrant of Fig. 2) for all points where $\omega_2 = \omega_{ba}$. That ridge is referred to as a singly resonant line with the resonance equation $\omega_2 = \omega_{ba}$. For the DOVE-Raman process, however, the vibrational level for b needs to be Raman-active and Δ_{ba} in Eq. (1) predicts a singly resonant line that runs diagonally since its resonance equation will be $\omega_1 - \omega_2 = \omega_{cb}$, or $y = mx - \omega_{cb}$ where $y = \omega_2$, $x = \omega_1$, and $m = 1$ (see the top right quadrant in Fig. 2).

Peaks in a 2DIR spectrum may appear at the point where two singly resonant lines produced by either a DOVE-IR process or a DOVE-Raman process intersect [i.e., two Δ's in Eqs. (1) or (2) equal Γ]. Points in the 2D plot where that occurs are *doubly resonant*. For example, doubly resonant peaks may be created in a coherent 2D spectrum if level c is an IR-active level that is coupled to the fundamental vibration at level b and if the transition dipole moments μ_{ba} (for DOVE-IR) and/or μ_{cb} (for DOVE-Raman) are nonzero. A simple example of such a case would be if level b was a fundamental vibration that is both IR-active and Raman-active and

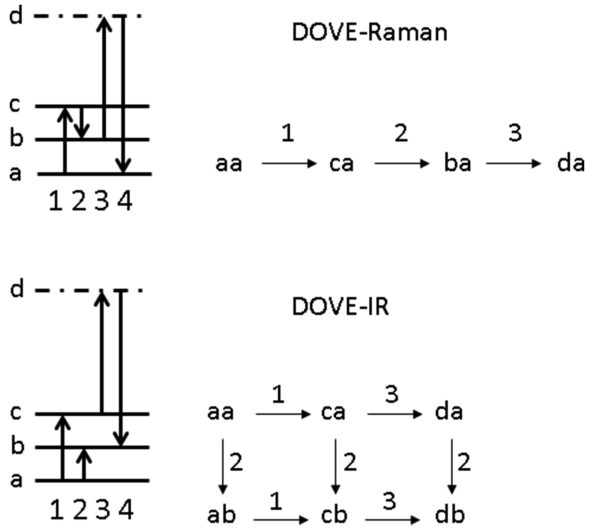

FIG. 1. Wave-mixing energy level diagrams (left) and Liouville diagrams (right) for DOVE-Raman (top) and DOVE-IR (bottom) FWM processes. These diagrams show the flow of coherence from the initial population state to the final coherence that launches the output beam. The DOVE-Raman process is parametric because the starting and ending levels are identical (level a). The DOVE-IR process is nonparametric because the process starts in level a but ends in level b. It includes two accompanying FWM pathways with different input photon orders: 2,1,3 and 1,3,2, as shown in its Liouville diagram. The combined contribution from all three DOVE-IR pathways is described by Eq. (2) in the text.

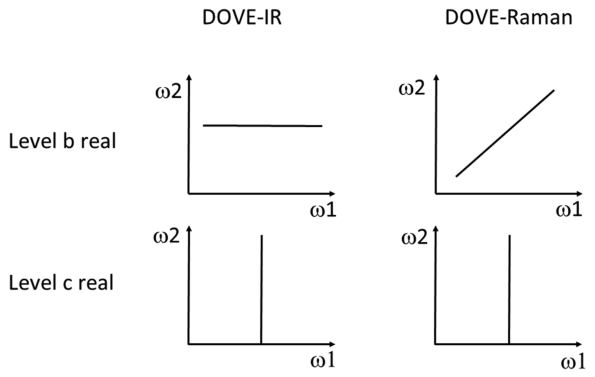

FIG. 2. A 2DIR spectrum can be displayed as a 1,2 plot if the intensity of the generated FWM signal (coming out of the page) is plotted as a function of ω_1 along the x-axis and ω_2 along the y-axis. This figure shows the orientation of singly resonant lines in 1,2 plots for four possible scenarios. The top left diagram illustrates that a singly resonant DOVE-IR process where level b is real (but levels c and d are virtual) can produce a horizontally resonant line based upon the resonance equation $\omega_2 = \omega_{ba}$ (see the text for more details). The top right diagram shows a diagonally oriented singly resonant line for the DOVE-IR process based upon the resonance equation $\omega_1 - \omega_2 = \omega_{cb}$. The bottom two diagrams show that if level c is real (and levels b and d are virtual), the resulting singly resonant line will be vertical for both DOVE-IR and DOVE-Raman.

level c was its IR-active overtone. In such a case, both DOVE-IR and DOVE-Raman peaks could be generated in the 2DIR spectrum.

To correctly interpret a HR-2DIR spectrum and assign its peaks, one needs to be able to distinguish between peaks produced by DOVE-IR and those produced by DOVE-Raman. In the condensed phase, the contribution from both processes can overlap and interfere because the anharmonicity is comparable to the linewidth of the vibrational peaks. In the gas phase, peak linewidths are small compared to the anharmonicity, so peaks from the two different processes may be clearly resolved and the contributions from the two FWM processes may appear to be clearly separated. Prior work on HRCMDS has shown that the shapes of the patterns and the way that the peaks are ordered by the rotational quantum number within the patterns depend upon which lasers are scanned and which FWM process produces the peaks. One possible way to distinguish between peaks produced by DOVE-IR and those produced by DOVE-Raman is to examine the orientation of the singly resonant lines that intersect to form these doubly resonant peaks in the 2D spectrum. For example, if levels b and c are the fundamental and overtone vibrations for the same vibrational mode, then their rovibrational peaks will be coupled for DOVE-Raman and DOVE-IR if that vibrational mode is both IR and Raman active and frequencies (ω_1 and ω_2) obey their corresponding rotational selection rules. Figure 2 shows that for a 1,2 plot where the x-axis is ω_1 and the y-axis is ω_2, the orientations of the resulting singly resonant rovibrational lines in the 2D plot will be different; the singly resonant DOVE-Raman lines will be vertical and diagonal while the DOVE-IR singly resonant lines will be vertical and horizontal.

Rotational selection rules also help in determining the structure of the 2D pattern in high resolution coherent 2D spectra. In the UV–VIS region, X-shaped patterns have been observed when $B' \approx B''$ and the rotational selection rule was $\Delta J = \pm 1$.[20] If the excited and ground electronic states have very different rotational constants, the branches of the X-shape become curved, resulting in a double parabola pattern.[40] For resonances in the infrared region, the differences in rotational constants among levels a, b, and c are likely to be smaller because the molecule's electronic configuration remains constant. Figure 3 shows simulated 2DIR patterns made with the assumption that the rotational constants for levels a, b, and c are the same. The resulting pattern resembles an asterisk for the rotational selection rule $\Delta J = 0, \pm 1$, which is common for infrared spectra of polyatomic molecules. The asterisk shape is produced by nine pairings: three values of ΔJ for ω_1 (corresponding to P, Q, and R) are paired with three values of ΔJ for ω_2. Each of the nine possibilities (PP, PQ, PR, QP, QQ, QR, RP, RQ, and RR) produces a different branch in the asterisk, except for the QQ peaks, where peaks accumulate to form an intense center. These nine branches are labeled on the DOVE-IR and DOVE-Raman asterisks in Fig. 3. For example, if $J = 0$ for level a (i.e., $J_a = 0$), then for DOVE-IR, J_b must be 0 or 1 and J_c must be 0 or 1 (i.e., there are four possibilities). The QQ branch in the center of the DOVE-IR asterisk is produced when both J_b and J_c are zero, the red QR peak is produced when $J_b = 1$ and $J_c = 0$, the red RQ peak is produced when $J_b = 0$ and $J_c = 1$, and the red RR peak is produced when $J_b = 1$ and $J_c = 1$. For $J_a \geq 1$, the number of peaks increases from 4 to 9, eight of which form a rectangle (see the gray peaks for $J_a = 1$ and the yellow peaks for $J_a = 2$). Higher values of J_a produce larger rectangles. For the DOVE-Raman process, the repeating pattern is a trapezoid rather than a rectangle.

In Fig. 3, the centers of the two asterisks have different y-axis values due to vibrational anharmonicity, which causes the resonance frequency of ω_2 needed for ω_{ba} (DOVE-IR) to be greater than that for ω_{cb} (DOVE-Raman). By contrast, the x-axis values for the two

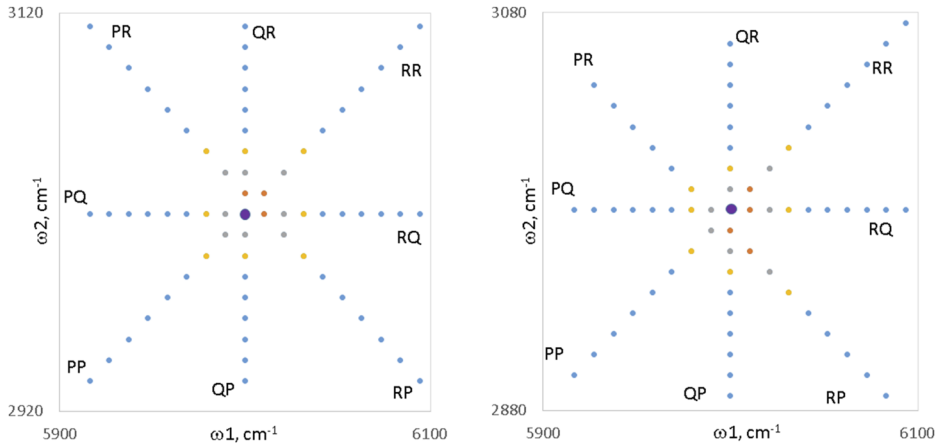

FIG. 3. 2DIR simulations showing 1,2 plots of DOVE-IR (left) and DOVE-Raman (right) rovibrational patterns, based upon the selection rule $\Delta J = 0, \pm 1$. The red, gray, and yellow peaks have ground level J_a values of 0, 1, and 2, respectively. The larger purple peak at the center of each asterisk marks the position of a group of peaks that have the same coordinate and that accumulate to form the QQ branch. The basic repeating pattern for $J_a \geq 1$ consists of nine peaks that have the same shape as the eight yellow peaks plus one peak in the QQ branch. The size of this basic repeating pattern grows systematically as J_a increases. For example, the basic pattern for the DOVE-IR process consists of eight peaks that form a rectangle (see the yellow peaks on the left asterisk) plus a peak inside of the QQ branch, and higher values of J_a produce larger rectangles. The basic repeating pattern for the DOVE-Raman process also consists of eight peaks plus a peak in the QQ branch, but the shape is a trapezoid (see the yellow peaks on the right asterisk). For this simulation, $\omega_{ba} = 3019\ cm^{-1}$ and $\omega_{ca} = 6000\ cm^{-1}$ and $B = 5.24\ cm^{-1}$ and the molecule was assumed to behave like a rigid rotor.

centers are similar because both the DOVE-IR and DOVE-Raman processes involve the same ω_{ca} resonance. The fact that the centers of the asterisks are displaced vertically but not horizontally should be useful for identifying which asterisks in HR-2DIR spectra involve the same vibration for level c, for determining the size of the anharmonicity, and for discerning which peaks come from DOVE-IR and which ones come from DOVE-Raman.

The simulation shows additional slight differences in the internal structure of the two asterisks. Each asterisk is composed of horizontal, vertical, and diagonal branches that intersect at a central point. For each asterisk, however, the diagonal branch with a negative slope does not pass through the central QQ point. For the DOVE-IR process, that diagonal branch travels above and to the right of the QQ point, and for the DOVE-Raman process, that diagonal branch travels below and to the left of the QQ point. The number of resonances is also different; the DOVE-IR rectangle has three ω_1 and three ω_2 values, while the DOVE-Raman trapezoid has three ω_1 values and seven ω_2 values.

In summary, these simulations show that there are several methods for determining whether an experimentally observed asterisk pattern is produced by the DOVE-IR or DOVE-Raman process, a determination that is needed to accurately interpret the results and assign rotational quantum numbers. First, since the peaks in the experimental HR-2DIR spectrum will be produced by the intersection of two singly resonant lines, examination of the FWM intensity around the base of the peaks can reveal the orientation of these lines. Comparison of these line orientations with those shown in Fig. 2 can then be used to determine whether the peak is from DOVE-IR or DOVE-Raman. At the base of each peak, these singly resonant line intensities should be increased by near-resonance enhancement, making them easier to see. Second, as described in the previous paragraph, the DOVE-Raman patterns and the DOVE-IR patterns have slightly different diagonals with a negative slope. Third, in the case of studies involving a fundamental vibration for level b and its overtone for level c, the QQ branch for the DOVE-IR asterisk will have a higher frequency than that for the DOVE-Raman asterisk. Finally, the DOVE-IR peaks are more susceptible to absorption effects because ω_1 and ω_2 photons connect the ground level a with levels c and b. For DOVE-Raman, however, absorption only affects ω_1 because ω_2 is resonant with levels b and c and does not involve ground level a (see Fig. 1). Therefore, as ω_2 is scanned, the intensity of the DOVE-IR peaks will be decreased by absorption at their peak resonance wavelengths ($\omega_2 = \omega_{ab}$), but the DOVE-Raman peaks will not because anharmonicity causes the absorption wavelengths to be different from the DOVE-Raman resonance wavelengths ($\omega_{ab} \neq \omega_{cb}$).

EXPERIMENTAL METHODS

Figure 4 shows a simplified experimental layout for the HR-2DIR spectrometer. To facilitate multichannel detection with a monochromator and CCD, a multiwavelength output beam in the visible region was generated by spatially and temporally overlapping three focused input beams: a broadband near IR optical parametric oscillator (OPO) for ω_1, a narrowband tunable mid-IR optical parametric oscillator/optical parametric amplifier (OPO/OPA) for ω_2, and a fixed wavelength visible beam (λ = 532 nm) for ω_3. The narrowband tunable mid-IR beam had a linewidth of ~0.2 cm^{-1} and

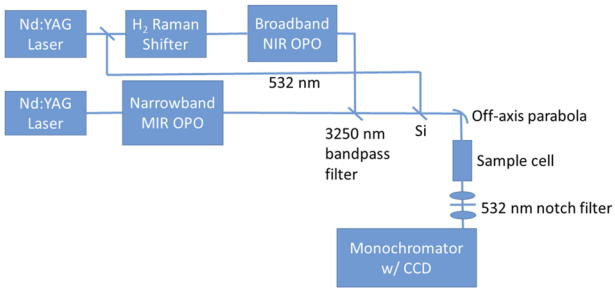

FIG. 4. Simplified experimental layout of the HR-2DIR spectrometer.

was produced using a LaserVision OPO/OPA that was pumped by an injection-seeded SpectraPhysics PRO-250 laser. The pump wavelength was 532 nm for the OPO stage and 1064 nm for the OPA stage. The broadband near IR OPO was pumped by the output of a hydrogen Raman shifter cell that was pumped by a beam of 532 nm light from an injection-seeded Nd:YAG laser (SpectraPhysics GCR-230). Operating an OPO near degeneracy causes its bandwidth to increase, and this BBO OPO was tuned slightly off degeneracy to produce idler beam photons of the range of 1400–1900 nm. A bandwidth with a FWHM of >400 cm^{-1} was inferred after recording a spectrum of the signal beam with a near IR spectrometer equipped with an InGaAs array detector. The 532 nm beam used for ω_3 came from the GCR-230 laser, and its exact wavelength (as well as the exact wavelength of the 532 nm beam from the PRO-250 laser) was measured to an accuracy of <0.004 nm using a 1.25 m monochromator equipped with a CCD.

The two IR beams were combined collinearly using a Thorlabs 3250 nm bandpass filter (bandwidth of 500 nm), and a silicon beamsplitter was used to combine them with the 532 nm beam. The three beams were then focused into the sample cell using an off-axis parabola with a focal length of 152.4 mm. The 10 cm pathlength static sample cell had CaF_2 windows and was filled with methane using an inflatable bag glove box so that the methane pressure was 1 atm. The beam energies at the cell were ~0.5 mJ for ω_1, 2.5 mJ for ω_2, and 0.25 mJ for ω_3. A strong multiplex CARS signal from methane (>50 000 counts per second at 460.6 nm) was used to optimize the spatial and temporal overlap of the three input beams. The generated FWM signal was detected using a 1.25 m monochromator (SPEX or JY 1250m) equipped with a 2400 g/mm grating and a 2048 × 512 element CCD (with 13.5 μm wide pixels). Typical collection times were less than an hour for a spectrum containing 3000 × 2048 points.

The wavelength produced by the tunable OPO system was calibrated by diverting a small portion of its beam reflected from the silicon beamsplitter into a 1.5 cm thick methane absorption cell and monitoring the intensity of the transmitted light during the scan. Dips in that transmittance spectrum were matched to peaks in a FTIR spectrum of methane. Light from a neon lamp was used to wavelength calibrate the monochromators.

RESULTS AND DISCUSSION

Figure 5 shows a HR-2DIR spectrum recorded by scanning the signal beam of the tunable narrowband OPO (that was not sent into

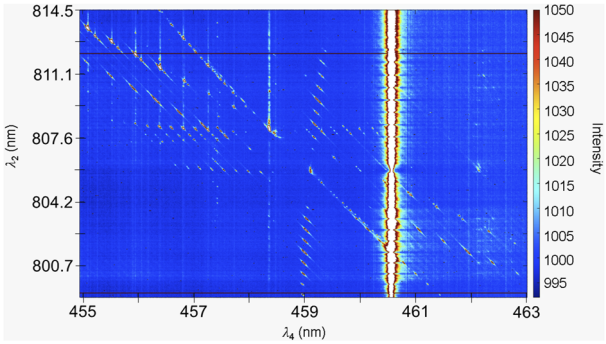

FIG. 5. Unprocessed HR-2DIR spectrum of methane (4,2 plot). The x-axis is the monochromator wavelength λ_4 and the y-axis is the tunable OPO signal beam wavelength λ_2. Features that look like they are created by vertical and diagonal singly resonant lines are encircled in a red oval and are attributed to the DOVE-Raman process. Features that are long and diagonal are encircled in yellow ovals and are attributed to the DOVE-IR process. The small black square encloses the QQ central branch for the DOVE-Raman asterisk while the small black circle encloses the QQ central branch for the DOVE-IR asterisk.

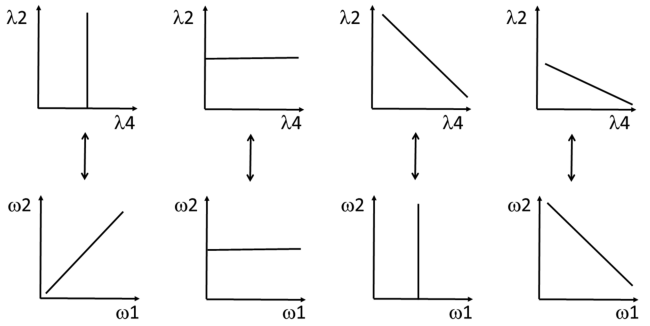

FIG. 6. Transforming the plot from 4,2, to 1,2 and vice versa changes the orientation of vertical, diagonal, and horizontal branches of peaks. These plots show how these orientations change and were produced by rearranging the FWM equation $\omega_4 = \omega_1 - \omega_2 + \omega_3$ and by converting between units of cm^{-1} and nm.

the cell) from 800.1 to 814.5 nm and monitoring the output beam intensity as a function of its wavelength (λ_4) with the monochromator centered at 459 nm. As a result, the corresponding narrowband OPA idler beam that was focused into the cell was scanned over a range of ~2880–3100 cm^{-1} so that it would be resonant with methane's symmetric and asymmetric CH-stretching modes. Meanwhile, the center of the broadband near-IR beam was set to approximately twice that frequency so that it would be resonant with the CH-stretching overtone at around 6005 cm^{-1}.

The saturated vertical line at the λ_4 detection wavelength of 460.6 nm is a singly resonant line that is attributed to a singly resonant FWM process that is similar to DOVE-Raman FWM, but with level c as a virtual level. The vibration responsible for this line is the symmetric CH stretch of methane (ν_1), which is Raman-active but not IR-active and is, therefore, unable to contribute peaks in the 2D spectrum. This feature is convenient for finding and optimizing the FWM signal because it can be found at the same detection wavelength for all wavelength values of the narrowband tunable OPO (λ_2) in the scan range. It also shows dips in intensity due to absorption whenever wavelength λ_2 is strongly absorbed by methane.

The peaks to the left and right of the 460.6 nm saturated singly resonant line are weaker in intensity by 1–2 orders of magnitude. These doubly resonant peaks are attributed to methane's asymmetric CH stretch (ν_3), which is IR-active and Raman-active. Some of these peaks appear to be created by vertical and diagonal (negative slope) singly resonant lines (see the red oval in Fig. 5) while others appear to be long, diagonal and negatively sloped (see the yellow ovals in Fig. 5). The diagrams in Fig. 2 predict that DOVE-IR peaks should be formed by the intersection of vertical and horizontal resonance lines and DOVE-Raman peaks should be formed by vertical and diagonal (positive slope) resonance lines. However, this prediction is for 1,2 plots (where the x-axis is ω_1 and the y-axis is ω_2). Figure 6 shows how singly resonant features in a 1,2 plot (in units of cm^{-1}) will appear if plotted using a 4,2 plot (where the x-axis is λ_4, the y-axis is λ_2, and the units are in nm) and vice versa. According to Fig. 6, the predicted orientation of singly resonant lines in a 4,2 plot becomes diagonal (negative slope) and horizontal for DOVE-IR and vertical and diagonal (negative slope) for DOVE-Raman. Therefore, the peaks enclosed in the red oval in Fig. 5 are attributed to DOVE-Raman. The peaks in the yellow ovals can be attributed to DOVE-IR if the absence of the horizontal resonance line is attributed to absorption. This attribution is supported by the observation that the y-axis values for the peaks in yellow ovals match the y-axis values of absorption dips observed in the saturated singly resonant line at 460.6 nm.

The small black square encloses the QQ central branch for the DOVE-Raman asterisk while the small black circle encloses the QQ branch for the DOVE-IR asterisk. These centers are surrounded by the other eight branches that comprise the asterisk pattern, but the asterisks appear asymmetric in the 4,2 plot. The symmetry of the asterisk can be restored by converting the 4,2 plot into a 1,2 plot that more closely resembles the simulations in Fig. 3. The procedure for this conversion involves converting the y-axis from near infrared wavelengths (of the OPO signal beam) to the mid-infrared wavenumber values (for the OPA idler beam) and transforming the x-axis from the monochromator wavelength to the corresponding ω_1 value in cm^{-1}. To carry out the latter step, a 2D peak picker (using a modified version of nmrDraw) was used to identify the x,y coordinate for each peak in the spectrum shown in Fig. 5. Those coordinates were then converted to cm^{-1} and the formula $\omega_1 = \omega_2 - \omega_3 + \omega_4$ was used to calculate the new x-axis value for each identified peak. The formula $\omega_2 = \omega_{\text{OPO signal beam}} - \omega_{1064}$ was used to calculate the new y-axis values.

The resulting 1,2 spectrum is shown in Fig. 7, next to a simulation that is similar to the one shown in Fig. 3. The combined transform of both axes (from 4,2 in nm to 1,2 in cm^{-1}) changed the orientation of the horizontal, vertical, and diagonal branches that connect related peaks in Fig. 5 in a way that agrees with that displayed in Fig. 6. Displaying the results as a 1,2 plot of the identified peaks also makes pattern recognition easier because the asterisk patterns appear to be more symmetrical in the 1,2 plot than they do in the 4,2 plot. The symmetry also makes it easy to distinguish between peaks from the DOVE-IR and DOVE-Raman processes and to identify important relationships. For example, the 1,2 plot allows one to clearly see which DOVE-IR peaks and DOVE-Raman peaks have

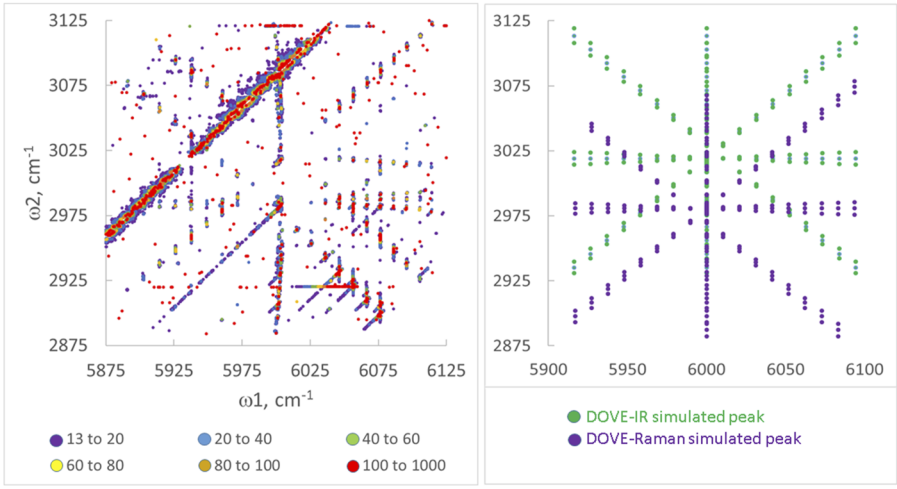

FIG. 7. The experimental HR-2DIR 1,2 plot in cm^{-1} on the left and the simulated HR-2DIR peaks from DOVE-IR (green peaks) and DOVE-Raman (purple peaks) for methane on the right. The simulation includes Coriolis splitting of the triply degenerate ν3 mode, which was observed in the experimental plot. Both plots show that both the DOVE-IR and DOVE-Raman processes produce highly symmetric asterisks that are separated along the y-axis but have many similar ω_1 values along the x-axis. These ω_1 values are useful for determining which photons in the ω_1 broadband beam were resonant with rovibrational levels in the overtone region that were coupled to the fundamental CH asymmetric vibration. Additional peaks in the experimental plot may be attributed to cosmic ray events (irreproducible) or contributions from other overtones or combination bands (reproducible). The solid diagonal line with a positive slope is a singly resonant line due to the ν1 symmetric CH vibration that does not contribute any peaks in the HR-2DIR spectrum (see the text). The horizontal lines just below ω_2 = 2875 and 3125 cm^{-1} are markers from a flash of light used to help calibrate the y-axis during the scan.

the same ω_1 values and, therefore, involve the same CH overtone rovibrational peaks for level c.

The simulated plot in Fig. 7 includes Coriolis effects that cause three-featured structures in both the experimental and simulated plots. The three features appear to be diagonally aligned (negative slope) in the 4,2 plot and vertically aligned in the 1,2 plot. Furthermore, the singly resonant CARS line for the symmetric CH stretch that was a vertical line in the 4,2 plot (Fig. 5) now appears as a diagonal line with a positive slope in the 1,2 plot. The change in orientations of these features also agree with that predicted by Fig. 6. Some of the peaks in Fig. 7 that are not in the simulation are due to cosmic rays hitting the CCD. However, others are reproducible and may be due to contributions from other combination bands or overtones. To assign these other peaks and extract molecular constants, a more detailed analysis of the positions of all peaks in this spectrum is currently underway and will be submitted for publication.

CONCLUSION

The ability to generate high resolution 2DIR spectra of gas phase molecules has been demonstrated for the first time. Peaks in the HR-2DIR spectra of methane are produced by either a DOVE-IR or DOVE-Raman process, each of which assembles the peaks into an asterisk pattern due to the rotational selection rule $\Delta J = 0, \pm 1$. Within each asterisk, all the peaks have the same vibrational quantum number but different rotational quantum numbers. The shape and structure of the DOVE-IR and the DOVE-Raman asterisks are slightly different. The way that the peaks are sorted by rotational quantum number also differs for the two FWM processes, so identification of the correct FWM process is essential for accurately assigning quantum numbers to the peaks. Pairs of asterisks produced by the same vibrational levels but different FWM processes align vertically but are displaced horizontally in 1,2 plots due to anharmonicity. The shapes of individual peaks can also be used to identify the FWM processes.

Splitting of the triply degenerate asymmetric CH stretch by the Coriolis effect is also observed in the HR-2DIR spectrum of methane. Methane has both symmetric and asymmetric CH stretches, but only the asymmetric stretch produces peaks in the HR-2DIR spectrum because it is both IR and Raman active. The symmetric stretch is IR inactive and Raman active, and, therefore, only generates a singly resonant line that runs vertically in the 4,2 plot and diagonally in the 1,2 plot. The 1,2 plot is generally more convenient to use for comparison with simulations, recognition of symmetric patterns, and identification of the ω_1 resonances (CH overtone peaks) that are coupled to the ω_2 resonances (CH fundamental vibration peaks). Additional features in the HR-2DIR spectra are observed that may be due to contributions from other overtones and/or combination bands.

The ability to record 2DIR spectra with higher spectral resolution should permit gas phase molecules to be studied in ways that could give greater insight into detailed molecular structures and behavior compared to traditional 1D methods, where spectral congestion and complexity have limited the ability to assign peaks by their quantum number and/or species. With a sufficiently high resolution monochromator, the x-axis resolution of the HR-2DIR technique would be limited by the linewidth of the 532 nm beam, which is <0.003 cm^{-1} due to injection seeding. Methane is a spherical rotor, and the HR-2DIR patterns produced by other kinds of rotors will form different kinds of patterns that might lead to additional capabilities and insight into molecular structures and behavior. The ability to analyze complex spectra at any temperature (without the

use of rotational cooling in a molecular jet) restores rotational information and expands applications of rovibrational spectroscopy to higher temperatures. This technique could potentially be useful for probing chemical reactions *in situ*, identifying different molecules in gaseous mixtures, and studying conformers and floppy molecules.

ACKNOWLEDGMENTS

The authors wish to thank Geronimo Villanueva for his helpful suggestions that contributed to the development of this technique and Kiera Daughtry for her assistance with recording spectra. This material is based on the work supported by the National Science Foundation under Grant No. NSF CHE-1832098. DeAunna Daniels was supported by funding from the Spelman College Chemistry and Biochemistry Scholars program.

AUTHOR DECLARATIONS

Conflict of Interest

The authors have no conflicts to disclose.

Author Contributions

D.A.D. planned experiments, recorded the spectra, and analyzed the results. T.A.W. helped in developing and testing the spectrometer. P.C.C. developed the concept and theory, supervised the project, and wrote the paper.

DeAunna A. Daniels: Data curation (equal); Formal analysis (lead); Investigation (equal); Methodology (equal); Validation (equal); Writing – review & editing (equal). **Thresa Wells**: Conceptualization (supporting); Investigation (supporting); Methodology (supporting); Validation (supporting); Writing – review & editing (equal). **Peter C. Chen**: Conceptualization (lead); Investigation (equal); Methodology (equal); Project administration (lead); Supervision (lead); Validation (supporting); Writing – original draft (lead).

DATA AVAILABILITY

The data that support the findings of this study are available from the corresponding author upon reasonable request.

REFERENCES

[1]L. Minnes, D. J. Shaw, B. P. Cossins, P. M. Donaldson, G. M. Greetham, M. Towrie, A. W. Parker, M. J. Baker, A. J. Henry, R. J. Taylor, and N. T. Hunt, Anal. Chem. **89**, 10898 (2017).
[2]Y. Feng, J. Huang, S. Kim, J. H. Shim, A. D. MacKerell, and N.-H. Ge, J. Phys. Chem. B **120**, 5325 (2016).
[3]R. Fritzsch, P. M. Donaldson, G. M. Greetham, M. Towrie, A. W. Parker, M. J. Baker, and N. T. Hunt, Anal. Chem. **90**, 2732 (2018).
[4]H. Sowley, Z. Liu, J. Davies, R. Peach, R. Guo, S. Sim, F. Long, G. Holdgate, K. Willison, W. Zhuang, and D. R. Klug, J. Phys. Chem. B **123**, 3598 (2019).
[5]L. Chuntonov and I. V. Rubtsov, J. Phys. Chem. C **126**, 3314 (2022).
[6]A. Ghosh, A. K. Prasad, and L. Chuntonov, J. Phys. Chem. Lett. **10**, 2481 (2019).
[7]L. Chuntonov and I. V. Rubtsov, J. Chem. Phys. **153**, 050902 (2020).
[8]N. H. C. Lewis and A. Tokmakoff, J. Phys. Chem. Lett. **12**, 11843 (2021).
[9]C. A. Tibbetts, A. B. Wyatt, B. M. Luther, and A. T. Krummel, in *ACS Symposium Series*, edited by M. R. Berman, L. Young, and H.-L. Dai (American Chemical Society, Washington, DC, 2021), pp. 109–134.
[10]W. Xiong, in *ACS Symposium Series*, edited by M. R. Berman, L. Young, and H.-L. Dai (American Chemical Society, Washington, DC, 2021), pp. 89–107.
[11]Z. Zhang, K. Wang, Z. Yi, M. S. Zubairy, M. O. Scully, and S. Mukamel, J. Phys. Chem. Lett. **10**, 4448 (2019).
[12]P. Saurabh and S. Mukamel, J. Chem. Phys. **144**, 124115 (2016).
[13]B. Guchhait, C. A. Tibbetts, K. M. Tracy, B. M. Luther, and A. T. Krummel, J. Chem. Phys. **152**, 164501 (2020).
[14]J. J. van Thor, J. Chem. Phys. **150**, 124113 (2019).
[15]L. M. Kiefer, J. T. King, and K. J. Kubarych, J. Phys. Chem. A **118**, 9853 (2014).
[16]J. D. Handali, K. F. Sunden, B. J. Thompson, N. A. Neff-Mallon, E. M. Kaufman, T. C. Brunold, and J. C. Wright, J. Phys. Chem. A **122**, 9031 (2018).
[17]S. Garrett-Roe and P. Hamm, Acc. Chem. Res. **42**, 1412 (2009).
[18]S. S. Mukherjee, D. R. Skoff, C. T. Middleton, and M. T. Zanni, J. Chem. Phys. **139**, 144205 (2013).
[19]P. C. Chen, J. Phys. Chem. A **114**, 11365 (2010).
[20]P. C. Chen and K. Mitchell, J. Chem. Phys. **129**, 194301 (2008).
[21]P. C. Chen and C. C. Joyner, Anal. Chem. **77**, 5467 (2005).
[22]P. C. Chen and C. C. Joyner, J. Phys. Chem. A **110**, 7989 (2006).
[23]P. C. Chen and M. Gomes, J. Phys. Chem. A **112**, 2999 (2008).
[24]Y. Suzuki and Y. Tanimura, J. Chem. Phys. **119**, 1650 (2003).
[25]J. Lu, Y. Zhang, H. Y. Hwang, B. K. Ofori-Okai, S. Fleischer, and K. A. Nelson, Proc. Natl. Acad. Sci. U. S. A. **113**, 11800 (2016).
[26]Y. Zhang, J. Shi, X. Li, S. L. Coy, R. W. Field, and K. A. Nelson, Proc. Natl. Acad. Sci. U. S. A. **118**, e2020941118 (2021).
[27]G. Kowzan and T. K. Allison, arXiv:2206.10488 (2022).
[28]G. Kowzan and T. K. Allison, arXiv:2206.10492 (2022).
[29]A. Mandal, G. Ng Pack, P. P. Shah, S. Erramilli, and L. D. Ziegler, Phys. Rev. Lett. **120**, 103401 (2018).
[30]J. C. Wright, J. Phys. Chem. Lett. **10**, 2767 (2019).
[31]P. C. Chen, T. A. Wells, and B. R. Strangfeld, J. Phys. Chem. A **117**, 5981 (2013).
[32]T. A. Wells, A. K. Muthike, J. E. Robinson, and P. C. Chen, J. Chem. Phys. **142**, 212426 (2015).
[33]T. A. Wells, V. J. Barber, M. H. Kwizera, P. Mukashyaka, and P. C. Chen, J. Phys. Chem. A **122**, 8794 (2018).
[34]B. R. Strangfeld, T. A. Wells, and P. C. Chen, J. Phys. Chem. A **118**, 6846 (2014).
[35]T. A. Wells, M. H. Kwizera, S. M. Chen, N. Jemal, M. D. Brown, and P. C. Chen, J. Chem. Phys. **154**, 194201 (2021).
[36]J. C. Wright, Anal. Chem. **92**, 8638 (2020).
[37]P. M. Donaldson, R. Guo, F. Fournier, E. M. Gardner, L. M. C. Barter, C. J. Barnett, I. R. Gould, D. R. Klug, D. J. Palmer, and K. R. Willison, J. Chem. Phys. **127**, 114513 (2007).
[38]P. Hamm and M. Zanni, *Concepts and Methods of 2D Infrared Spectroscopy* (Cambridge University Press, Cambridge, England, 2011).
[39]W. Zhao and J. C. Wright, J. Am. Chem. Soc. **121**, 10994 (1999).
[40]P. C. Chen, Appl. Spectrosc. **70**, 1937 (2016).